

Digital fast pulse shape and height analysis on cadmium–zinc–telluride arrays for high-flux energy-resolved X-ray imaging

Leonardo Abbene,^{a*} Fabio Principato,^a Gaetano Gerardi,^a Manuele Bettelli,^b Paul Seller,^c Matthew C. Veale,^c Nicola Zambelli,^d Giacomo Benassi^d and Andrea Zappettini^b

Received 18 May 2017

Accepted 27 October 2017

Edited by P. A. Pianetta, SLAC National Accelerator Laboratory, USA

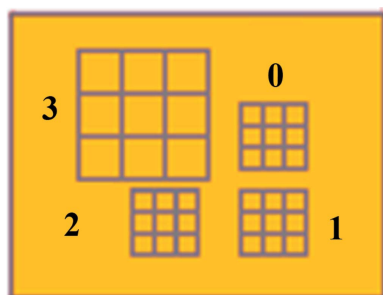
Keywords: digital pulse shape analysis; X-ray and γ -ray detectors; CdZnTe detectors; high flux; charge sharing; energy-resolved photon counting detectors.

^aDipartimento di Fisica e Chimica, University of Palermo, Viale delle Scienze, Edificio 18, Palermo 90128, Italy, ^bIMEM/CNR, Parco Area delle Scienze 37/A, Parma 43100, Italy, ^cScience and Technology Facilities Council, Rutherford Appleton Laboratory, Chilton, Oxfordshire OX11 0QX, UK, and ^ddue2lab s.r.l., Via Paolo Borsellino 2, Scandiano, Reggio Emilia 42019, Italy. *Correspondence e-mail: leonardo.abbene@unipa.it

Cadmium–zinc–telluride (CZT) arrays with photon-counting and energy-resolving capabilities are widely proposed for next-generation X-ray imaging systems. This work presents the performance of a 2 mm-thick CZT pixel detector, with pixel pitches of 500 and 250 μm , dc coupled to a fast and low-noise ASIC (PIXIE ASIC), characterized only by the preamplifier stage. A custom 16-channel digital readout electronics was used, able to digitize and process continuously the signals from each output ASIC channel. The digital system performs on-line fast pulse shape and height analysis, with a low dead-time and reasonable energy resolution at both low and high fluxes. The spectroscopic response of the system to photon energies below (^{109}Cd source) and above (^{241}Am source) the K -shell absorption energy of the CZT material was investigated, with particular attention to the mitigation of charge sharing and pile-up. The detector allows high bias voltage operation ($>5000\text{ V cm}^{-1}$) and good energy resolution at moderate cooling (3.5% and 5% FWHM at 59.5 keV for the 500 and 250 μm arrays, respectively) by using fast pulse shaping with a low dead-time (300 ns). Charge-sharing investigations were performed using a fine time coincidence analysis (TCA), with very short coincidence time windows up to 10 ns. For the 500 μm pitch array (250 μm pitch array), sharing percentages of 36% (52%) and 60% (82%) at 22.1 and 59.5 keV, respectively, were measured. The potential of the pulse shape analysis technique for charge-sharing detection for corner/border pixels and at high rate conditions (250 kcps pixel^{-1}), where the TCA fails, is also shown. Measurements demonstrated that significant amounts of charge are lost for interactions occurring in the volume of the inter-pixel gap. This charge loss must be accounted for in the correction of shared events. These activities are within the framework of an international collaboration on the development of energy-resolved photon-counting systems for high-flux energy-resolved X-ray imaging (1–140 keV).

1. Introduction

Recently, great efforts have been made in the development of imaging arrays, with single-photon counting and energy-resolving capabilities, for colour/spectroscopic X-ray imaging (Norlin *et al.*, 2008; Taguchi & Iwaczyk, 2013; Tomita *et al.*, 2004), opening new perspectives for applications within the fields of diagnostic medicine, synchrotron applications, non-destructive testing (NDT) and security screening. Energy-resolved photon-counting (ERPC) arrays are typically based on high- Z and wide-band-gap direct-conversion compound semiconductors [gallium arsenide, cadmium telluride,



cadmium–zinc–telluride (CZT)] (Abbene *et al.*, 2015; Barber *et al.*, 2015; Iwanczyk *et al.*, 2009; Szeles *et al.*, 2008; Veale *et al.*, 2014a), able to ensure room-temperature operation and higher detection efficiency than the traditional semiconductor detectors (silicon, germanium) (Del Sordo *et al.*, 2009; Owens & Peacock, 2004; Takahashi & Watanabe, 2001). Silicon drift detectors (SDD), invented in 1984 by Gatti and Rehak (Gatti & Rehak, 1984; Gatti *et al.*, 1984), are also proposed for room-temperature spectroscopic X-ray imaging, representing the best solution up to 20 keV (Bertuccio *et al.*, 2015). Despite their excellent energy resolution and high detection efficiency, few ERPC prototypes based on high-purity germanium (HPGe) detectors have been developed, mainly due to their cumbersome cryogenic cooling (liquid and mechanical coolers) and the difficulties in fabricating small pixel devices (Johnson *et al.*, 2015; Campbell *et al.*, 2013; Krings *et al.*, 2015).

Due to the high-flux conditions of several imaging applications ($\geq 10^6$ photons $\text{mm}^{-2} \text{s}^{-1}$), the development of high-resolution ERPC systems must take into account several critical issues. Radiation-induced polarization, dead-time, pile-up and charge-sharing distortions are the main drawbacks. High-flux radiation-induced polarization phenomena (Abbene *et al.*, 2016; Bale & Szeles, 2008; Sellin *et al.*, 2010; Strassburg *et al.*, 2011) depend mainly on the characteristics of the detectors and high bias voltage operation, and good charge-transport properties (mobility lifetime products of holes and electrons) are required. The mitigation of the effects of dead-time, pile-up and charge sharing is, generally, the main task of pulse mode electronics and encouraging results are obtained through both analogue (Barber *et al.*, 2015; Iwanczyk *et al.*, 2009; Taguchi *et al.*, 2010) and digital approaches (Brambilla *et al.*, 2013; Streicher *et al.*, 2015). A common strategy, widely used by several groups (Barber *et al.*, 2015; Brambilla *et al.*, 2013; Iwanczyk *et al.*, 2009; Ogawa *et al.*, 2012), is to perform a fast shaping analysis on the detector pulses (*i.e.* the output pulses from the charge-sensitive preamplifier, CSP), thus providing shaped pulses with very short time widths (less than 500 ns). At high fluxes, the short time widths of the shaped pulses ensure low dead-time distortions, high throughputs, significant reduction of the pile-up effects and moderate spectral degradations. However, two issues must be considered when fast shaping is used: (i) the leading edge of the CSP pulses must be preserved to avoid ballistic deficit effects (Knoll, 2000) and so the minimum time width of the shaped pulses is related to the peaking time of the CSP pulses (which depends on the detector thickness, bias voltage, time response of the preamplifier, *etc.*); and (ii) fast shaping generally gives a lower signal-to-noise ratio (SNR) than long shaping; indeed, the energy spectra from a fast shaping analysis are typically characterized, even at low rates, by modest energy resolution, with typical values ranging between 8 and 20% FWHM at 60 keV (Barber *et al.*, 2015; Brambilla *et al.*, 2009; Baumer *et al.*, 2008; Greenberg *et al.*, 2016; Ogawa *et al.*, 2012).

Recently, within a research collaboration between the Department of Physics and Chemistry (DiFC) of the University of Palermo, Italy, the IMEM–CNR of Parma, Italy, and the

Rutherford Appleton Laboratory (RAL), Didcot, UK, we proposed to develop ERPC prototypes based on CZT pixel detectors for high-flux X-ray imaging applications. Within the framework of these activities, we developed, as the first step, some CZT pixel prototypes of different thicknesses and pixel pitches. The detectors are coupled to a fast and low-noise application-specific integrated circuit (ASIC) (Allwork *et al.*, 2012; Veale *et al.*, 2011) characterized only by the preamplifier stage. The output waveforms from the ASIC are analysed by a custom-designed digital pulse processing (DPP) electronics able to perform on-line fast pulse shape and height analysis (event arrival time, pulse shape, pulse height, *etc.*) with a low dead-time and a reasonable energy resolution at low and high fluxes (Abbene *et al.*, 2015; Abbene & Gerardi, 2015; Gerardi & Abbene, 2014).

In this work, we present the results of spectroscopic investigations on a 2 mm thick CZT pixel detector characterized by arrays of different pitch sizes, with particular attention to the mitigation of charge-sharing effects at both low and high fluxes.

2. CZT pixel detector

A CZT pixel detector with different anode arrays was fabricated by IMEM–CNR (Parma, Italy; <http://www.imem.cnr.it>) and due2lab s.r.l (Reggio Emilia, Italy; <http://www.due2lab.com>). The detector is based on a CZT crystal ($4.25 \times 3.25 \times 2$ mm), grown by Redlen Technologies (Victoria BC, Canada; <http://redlen.ca>) using the travelling heater method (THM) technique (Awadalla *et al.*, 2014; Chen *et al.*, 2007, 2008). Gold electroless contacts were realized on both the anode and the cathode of the detectors. A 4% AuCl₃ methanol solution, with a deposition time of 1 min at 25°C, was used (Benassi *et al.*, 2017). The anode pattern was obtained by photolithography and the passivation procedure was performed with an aqueous solution of H₂O₂ at 10% for 5 min, in order to reduce surface leakage currents. CZT detectors with gold electroless contacts are widely fabricated at IMEM–CNR and they are characterized by low leakage currents at room temperature (<5 nA cm^{-2} at 1000 V cm^{-1}) (Abbene *et al.*, 2017, 2016). Concerning the geometric layout of the detector, the anode surface is characterized by four arrays of 3×3 pixels with pixel pitches of 500 and 250 μm , surrounded by a guard-ring electrode (Fig. 1 and Table 1), while the cathode is a planar electrode covering the detector surface ($4.25 \times 3.25 \times 2$ mm). The width of the inter-pixel gaps for all arrays is 50 μm . The proposed design allows investigation of the different anode geometries in a single piece of CZT material.

3. Charge sharing and cross talk in pixellated CZT detectors

As widely reported in the literature (Barret *et al.*, 1995; Mardor *et al.*, 2001; He, 2001), CZT detectors with pixellated anodes are characterized by electron-sensing properties (the small-pixel effect) (Barret *et al.*, 1995), which are very

Table 1

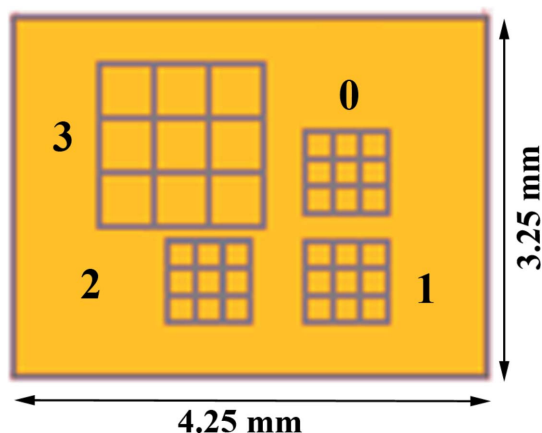
The geometric characteristics of the anode arrays of the CZT pixel detector.

Arrays 0 and 2 have the same geometric features as array 1.

Array No.	Pixel size a (μm)	Inter-pixel gap g (μm)	Pixel area A (pitch area) (mm^2)	Gap area G (mm^2)	G/A ratio (%)
1	200	50	0.0625	0.0225	36
3	450	50	0.2500	0.0475	19

important to minimize the effects of poor hole transport properties in the detector signal. This effect is due to the particular shape of the weighting potential generated by the pixel anode layout: it is low near the cathode and rises rapidly close to the anode. Therefore, in agreement with the Shockley–Ramo theorem (He, 2001; Knoll, 2000; Ramo, 1939; Shockley, 1938), the charge induced on the collecting pixel, proportional to the weighting potential, is mostly contributed from the drift of charge carriers close to the pixel, *i.e.* the electrons. Moreover, according to the small-pixel effect, this unipolar effect is enhanced by decreasing the ratio between the pixel size and the detector thickness. The main drawback of pixellated CZT detectors is represented by the spectral and spatial distortions caused by charge-sharing and cross-talk phenomena. The effects of these phenomena on the response of CZT/CdTe pixel detectors have been studied extensively through both theoretical (Chen *et al.*, 2002; Guerra *et al.*, 2008; Iniewski *et al.*, 2007; Xu *et al.*, 2011) and experimental approaches (Brambilla *et al.*, 2012, 2013; Bolotnikov *et al.*, 2016; Kim *et al.*, 2011; Kuvvetli *et al.*, 2007; Meuris *et al.*, 2009; Veale *et al.*, 2014b).

Before introducing these effects on the detector performance, we would like to set out the terminology for the nature of the output pulses from a CSP. Generally, the CSP output pulses are classified as collected- and induced-charge pulses. The collected-charge pulses are generated by the charge carriers actually collected by the pixel, while the induced-charge pulses are generated by the induced charge, collected


Figure 1

The anode layout of the CZT pixel detector. Array 3 is characterized by a pixel pitch of 500 μm , and arrays 0, 1 and 2 by a pixel pitch of 250 μm . All arrays are surrounded by a guard-ring electrode up to the edge of the crystal.

by another pixel. Generally, charge sharing refers to the splitting of the electron charge cloud generated from a single photon and collected by the neighbouring pixels. When charge sharing occurs in the inter-pixel gap, the contributions of both induced and collected charges can also co-exist in a single pulse.

Typically, charge sharing is due to charge diffusion, Coulomb repulsion, K -shell fluorescence and Compton scattering. Cross-talk events between neighbouring pixels are created by K -shell fluorescence, Compton scattering and induced pulses.

3.1. Electron cloud broadening

The initial size of the electron cloud is generally related to the range of the photoelectron ejected by the photoelectric interaction of X-rays (Bolotnikov *et al.*, 2007; Kalemci & Matteson, 2002). At photon energies less than 60 keV, the initial size (FWHM) of the electron cloud (modelled with a three-dimensional Gaussian function) can be neglected, since it is generally lower than 5 μm (Bolotnikov *et al.*, 2007; ESTAR, <http://physics.NIST.gov/PhysRefData/Star/Text/ESTAR.html>). The broadening of the electron cloud is mainly due to charge diffusion, Coulomb repulsion, K -shell fluorescence and Compton scattering. Due to diffusion (Bolotnikov *et al.*, 2007; Kim *et al.*, 2011), the cloud expands after drifting through the thickness of the detector. The size of the electron cloud, s , can be approximated by a Gaussian distribution (Bolotnikov *et al.*, 2007; Kim *et al.*, 2011)

$$s(\text{FWHM}) = 2.35 \left(\frac{2kT dL}{eV} \right), \quad (1)$$

where k is the Boltzmann constant, T is the absolute temperature, d is the drift distance, L is the detector thickness, e is the charge of the electrons and V is the cathode bias voltage. Using equation (1), the electron cloud sizes (at $T = 5^\circ\text{C}$, $L = 2$ mm and $V = 1200$ V) are calculated to be about 29 and 28 μm at 22.1 and 59.5 keV, respectively. At photon energies < 60 keV, the effects of Coulomb repulsion and Compton scattering can be neglected.

Another major reason for cloud spreading is related to the secondary products of X-ray interaction in the material. This includes the emission of K -edge characteristic X-rays which are reabsorbed far from the original interaction point. Indeed, at energies greater than the K -shell absorption energy of the CdZnTe material (Table 2), fluorescent X-rays are also emitted (approximately 70% of all photoelectric absorptions in the CZT material result in K -edge characteristic X-rays) (Shikhaliyev *et al.*, 2009). Fluorescent X-rays, due to their significant attenuation lengths (Table 2), broaden the initial electron cloud and can also create cross-talk events in neighbouring pixels (side and back escape events).

3.2. Weighting potential cross talk

The movement of the electron cloud over a collecting pixel will also induce a small signal on the surrounding non-collecting pixels. This effect is known as weighting potential

Table 2

The attenuation length λ_{CdZnTe} of K-shell fluorescent X-rays in CdZnTe materials (Berger *et al.*, 1998).

Element	K-shell absorption energy (keV)	Fluorescent lines	Energy of fluorescent lines (keV)	λ_{CdZnTe} (μm)
Cd	26.7	$K\alpha_1$	23.17	116
		$K\beta_1$	26.10	161
Zn	9.7	$K\alpha_1$	8.54	8.4
		$K\beta_1$	9.57	11.4
Te	31.8	$K\alpha_1$	27.47	69
		$K\beta_1$	31.00	95

cross talk (Guerra *et al.*, 2008; Brambilla *et al.*, 2012) and the induced-charge pulses are also termed transient pulses (Bolotnikov *et al.*, 2016; Kim *et al.*, 2011). The transient pulses are created by the particular shape of the weighting potential of a pixel detector, which is characterized by non-zero values even for interaction far from the collecting pixel. Fig. 2 shows the weighting potential of the central pixel (orange pixel) for the large array (500 μm) at different interaction points, up to the centre of the adjacent pixel (green pixel). The weighting potential was calculated by solving the Laplace equation (COMSOL *Multiphysics* software; <https://www.comsol.com/>). From Fig. 2, even for event charges fully collected by the adjacent pixel (green pixel), a small induced-charge pulse will also be created on the orange pixel. These transient pulses are generally characterized by a different shape from the typical collected-charge pulses: they rise as the electron cloud moves to the collecting pixel and then rapidly decrease to zero as the electrons are collected (Brambilla *et al.*, 2012; Bolotnikov *et al.*, 2016; Kim *et al.*, 2011).

3.3. Analytical modelling of charge sharing

Charge sharing in pixellated CZT detectors has been studied extensively using numerical simulations, with valida-

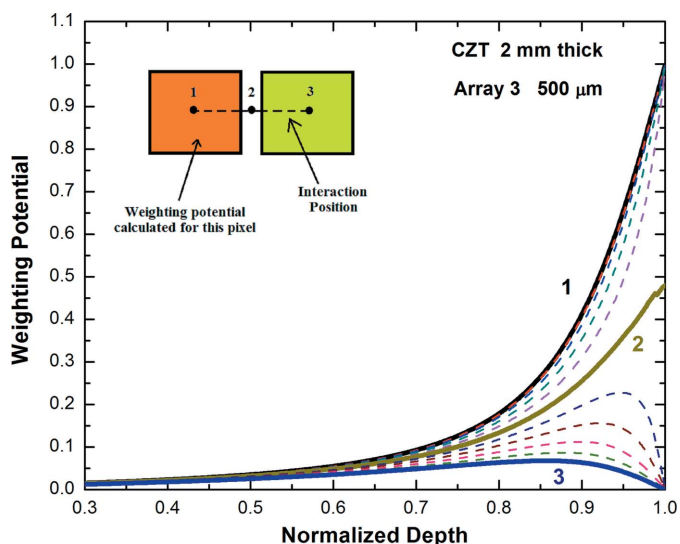


Figure 2
The weighting potential of the central pixel (orange pixel) of array 3 at different interaction points, up to the centre of the adjacent pixel (green pixel).

tions through experimental measurements. Since shared events mainly occur with photon interactions near the inter-pixel gap, a coarse approximation of the percentage of shared events between adjacent pixels can be simply given by the ratio of the inter-pixel gap area to the total detector area. Iniewski *et al.* (2007) have proposed an analytical model to calculate the probability of shared events through the geometric characteristics of the detectors, taking electron cloud broadening into account. Experimental validations of the model have been presented by several groups (Kuvvetli *et al.*, 2007; Meuris *et al.*, 2009; Veale *et al.*, 2014b). According to this model (Iniewski *et al.*, 2007), the probability P of sharing between two adjacent pixels is given by the following relation:

$$P(\text{sharing}) = 1 - \frac{(a + 2c - s)^2}{(a + g)^2}, \quad (2)$$

where a is the pixel size, g is the inter-pixel gap and s is the diameter of the electron cloud. The parameter c is the collection width describing the width over which a pixel collects the total charge deposited in an interaction (Iniewski *et al.*, 2007), and for a small inter-pixel gap it can be expected to be close to $0.5g$ (Veale *et al.*, 2014b). Thus, in our modelling we used a value of $0.5g$. Of course, equation (2) only gives a first-order approximation of the shared events, because it does not take into account the effects of fluorescence. However, it can be very helpful in a preliminary estimation of charge-sharing events, especially during the design of detector arrays.

3.4. Charge sharing and cross-talk effects

Generally, charge sharing and cross talk in pixel detectors produce distortions on the detection efficiency and degradations of the spectroscopic performance, *e.g.* by introducing tailing, fluorescence and associated escape peaks and a low-energy background into the measured spectra. These effects depend on both the physical (electric field, size and drift of the charge cloud, surface conductivity of the inter-pixel gap) and geometric (pixel size, inter-pixel gap, thickness) features of the detectors. Detection of charge-sharing events is generally performed through a time coincidence analysis (TCA), *i.e.* by detecting the events of adjacent pixels that are in temporal coincidence within a selected coincidence time window (CTW). The effects of charge sharing can be strongly mitigated through charge-sharing discrimination (CSD) techniques, *i.e.* by rejecting pulses in temporal coincidence. To recover the rejected shared events and so enhance the throughput, charge-sharing addition (CSA) techniques, which consist of summing the energies of the coincidence events, are also used (Allwork *et al.*, 2012; Kuvvetli *et al.*, 2007; Meuris *et al.*, 2009; Veale *et al.*, 2014b). However, in many cases, the energy obtained after summing the coincidence pulses of two adjacent pixels is lower than the correct value (Allwork *et al.*, 2012; Brambilla *et al.*, 2012; Bolotnikov *et al.*, 1999, 2002; Gaskin *et al.*, 2003; Kalemci & Matteson, 2002; Kim *et al.*, 2011; Kuvvetli *et al.*, 2007). Several explanations have been given for the presence of charge losses after CSA: (i) a non-zero energy threshold of the electronics; (ii) electric field distortions in the

inter-pixel gap (Bolotnikov *et al.*, 1999, 2002); and (iii) the simultaneous presence of both collected- and induced-charge contributions in the shared pulses between adjacent pixels (Kim *et al.*, 2011). Concerning the first explanation, when charge sharing occurs a small amount of charge may be collected by a pixel but be below the energy threshold so it will not be detected. Charge can also be physically lost in the gap between pixels where electric field distortions are present (Bolotnikov *et al.*, 1999, 2002, 2014). In many cases, due to the high conductivity of the surface compared with that of the bulk, some fraction of the electron cloud can reach the surface between adjacent pixels and thus not be collected by the pixel. These losses can be reduced by decreasing the size of the inter-pixel gaps or by using steering electrodes between the pixels (Abbene *et al.*, 2007; Kalemci & Matteson, 2002). The third explanation is related to the presence of the induced-charge contribution to the collected-charge pulse after charge sharing. Whenever charge sharing occurs, both collected- and induced-charge (transient) signals are generated on the neighbouring pixels. The transient contribution can alter the collected-charge signal by lowering the total energy after summing. When charge sharing does not occur, an interaction near the edge of the pixel can also create a transient pulse on the adjacent pixel, thus generating false signals that increase the total energy after summing (Kim *et al.*, 2014).

Particular care must be taken when charge-sharing detection in CZT pixel detectors is performed at high rate conditions. At high rates, the TCA can fail in detecting charge sharing, due to the high probability of the true coincidence of photons interacting simultaneously on neighbouring pixels. In these circumstances, pulse shape analysis (PSA) can be an appealing approach. Because shared pulses from the CSPs are characterized by different peaking times (*i.e.* different pulse shapes) compared with single pulses (Abbene *et al.*, 2015; Bolotnikov *et al.*, 2016; Brambilla *et al.*, 2012), this information can be very helpful to detect shared events.

In this work, we will show the results of charge-sharing detection, at low and high rates, using both the TCA and PSA techniques.

4. Electronics

4.1. Front-end electronics: the PIXIE ASIC

The detector is dc coupled to a fast and low-noise ASIC (PIXIE ASIC), recently developed at RAL (Allwork *et al.*, 2012; Veale *et al.*, 2011). The PIXIE ASIC consists of four arrays of 3×3 pixels, flip-chip bonded directly to the detector pixels. The active circuitry of each pixel is a CSP (with no shaping filter) and an output buffer which is multiplexed directly off the chip. The nine outputs from each of the four arrays are multiplexed onto a common nine-track analogue bus which is driven off-chip by the output buffers. The outputs of all nine pixels of the selected array are read out simultaneously, allowing analysis of the height and shape of the output pulses from the CSPs. The ASIC has two selectable ranges: a high-gain mode sensitive up to 150 keV and a low-

gain mode that allows measurements up to 1.5 MeV. To prevent saturation of the CSP waveforms at high rates, we used the low-gain mode. A calibration circuit in the central pixel of each array allows a pulser signal to be passed through the CSP. The feedback circuit was designed to provide detector leakage-current immunity of up to 250 pA per pixel. The pulses are characterized by rise times of less than 60 ns and a noise level (ENC) of less than 80 electrons. The bonding process was performed at RAL using low-temperature curing ($<150^\circ\text{C}$) *via* the silver-loaded epoxy and gold stud-bonding technique (Schneider *et al.*, 2015).

4.2. Digital electronics

The output waveforms from the PIXIE ASIC are digitized and processed by custom digital electronics. The digital system was recently developed at the DiFC of the University of Palermo and a detailed description is reported in our previous work (Abbene *et al.*, 2013, Abbene & Gerardi, 2015; Gerardi & Abbene, 2014). The digital electronics is able to perform a real-time pulse shape and height analysis (event arrival time, pulse height, pulse time width *etc.*) of the CSP waveforms, even at high rates and different throughput and energy-resolution conditions. The digital system (Fig. 3) consists of four digitizers (DT5724, 16 bit, 100 MS s^{-1} , CAEN S.p.A., Italy; <http://www.caen.it>) and a PC, through which the user can control all the digitizer functions, the acquisition and the analysis. The digitizers are connected and synchronized to realize a digitizing system with 16 channels (Fig. 3).

The digital pulse processing (DPP) analysis is performed using custom DPP firmware uploaded to the digitizers. The DPP firmware is able to perform two different shaping analyses: a fast and a slow pulse shape and height analysis (PSHA). In this work, to ensure high throughputs even at high rates, we only used the fast PSHA. Despite the short time widths of the output shaped pulses, the fast shaping analysis



Figure 3

The 16-channel digital readout electronics. The central box is the clock splitter used to synchronize all digitizers.

allows reasonable energy resolution at both low and high rates.

The digital analysis starts with the shaping of the output waveform from the detector ASIC using the classical single delay line (SDL) shaping technique (Knoll, 2000). SDL shaping is obtained by subtracting from the original pulse its delayed and attenuated fraction. SDL shaping gives short rectangular output pulses with fast rise and fall times (Fig. 4a). Generally, two main features characterize SDL shaping: (i) the time width of each SDL shaped pulse is well defined (delay time + CSP peaking time); and (ii) if the delay time is greater than the peaking time of the preamplified pulse, the SDL shaping also preserves the leading edge (pulse height and peaking time) of each CSP output pulse. These features make SDL shaping very appealing for timing and PSHA at both low and high rates. To increase the SNR we also performed a

further shaping with a trapezoidal filter (Fig. 4a). Through the fast PSHA, the system is able to provide, for each CSP pulse, the following results, recorded and presented in list mode:

- (i) the arrival time;
- (ii) the height of the fast SDL shaped pulses after baseline restoration and trapezoidal filtering, *i.e.* the energy of each event;
- (iii) the time width (*i.e.* the pulse shape) of the fast SDL shaped pulses; as widely shown in our previous work (Abbene *et al.*, 2015, 2017), the time width (TW) of the fast SDL shaped pulses and its relation to the pulse height can be very helpful for improving the detector performance.

To minimize the effects of baseline shifts in the measured spectra, especially at high rates, the system performs a fast baseline recovery using the running average of a fixed number of samples preceding the SDL pulse, where no further pulses are present.

An important feature of the digital system is that the dead-time is well defined. The time width of the pulses from fast shaping is a dead-time for the system, following a well known model (paralysable dead-time) (Knoll, 2000). In particular, the fast PSHA is characterized by a dead-time equal to the mean of the time widths of the fast shaped pulses. As shown in our previous work (Abbene & Gerardi, 2015), the true input counting rate (ICR) can be estimated from an exponential best fit of the measured time-interval distribution (TID) of the fast shaped pulses, or by inverting the throughput formula of the fast analysis (paralysable model).

The system can also provide a sequence of CSP output pulses together with the related arrival times, within selected time windows (snapshots) centred on each pulse peak position. This working mode is very helpful for performing a quick look and further off-line analysis on the CSP output pulses.

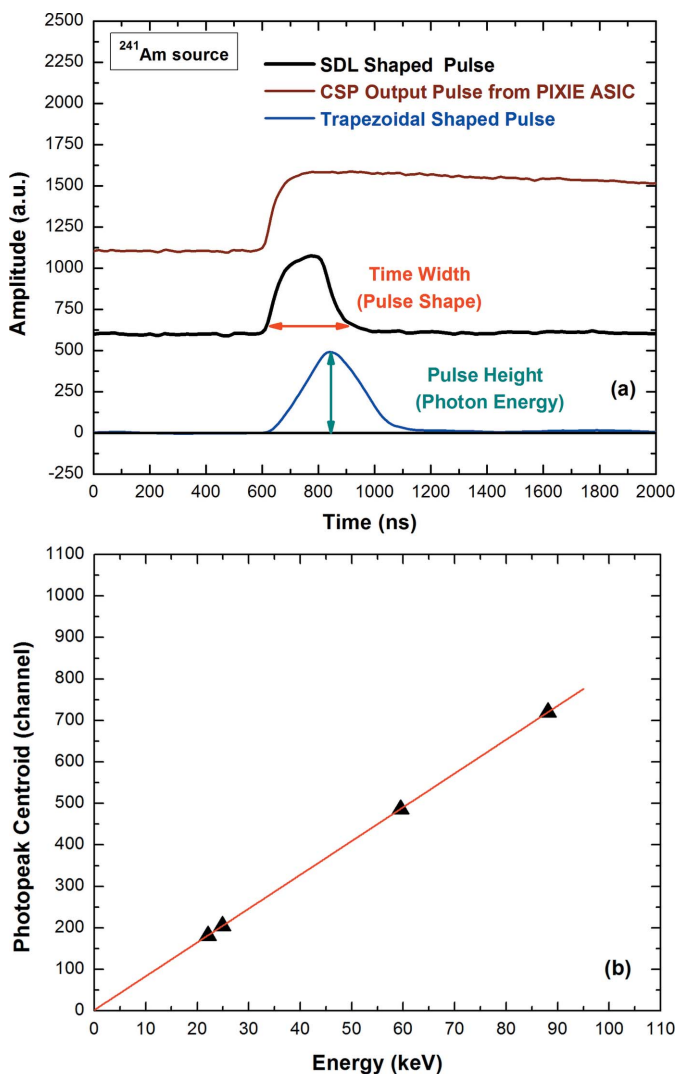


Figure 4
 (a) A typical CSP pulse from the PIXIE ASIC (brown line) and from the digital system after fast SDL shaping (black line) with a delay time of 200 ns and after trapezoidal filtering (blue line). (b) The centroid of the pulse height spectrum after fast shaping at different photon energies. The non-linearity is less than 0.1%, showing that fast shaping does not produce ballistic deficit effects. The measurements were performed at room temperature and with a bias voltage of 1000 V.

5. Experimental procedures

The detector was exposed, through the cathode side, to uncollimated X-ray and γ -ray calibration sources with energies above and below the K-shell absorption energy of the CZT material. We used ^{241}Am (main γ line at 59.5 keV, with the Np L X-ray lines shielded by the source holder) and ^{109}Cd (X-ray lines at 22.1 and 24.9 keV and γ line at 88.1 keV) sources. To obtain different ICRs of the impinging photons on the detector (through the cathode surface), we changed the solid angle subtended by the detectors, *i.e.* the distance from the sources to the detectors.

To avoid the effects of ballistic deficit and nonlinearity (Knoll, 2000), we used a delay time of 200 ns, greater than the peaking time of the CSP pulses (180 ns). Fig. 4(a) shows a typical CSP pulse from the PIXIE ASIC, the related fast SDL shaped pulse and the pulse after trapezoidal shaping. The linearity of the fast analysis was also verified experimentally (Fig. 4b).

To prevent saturation of the CSP waveforms at high rates, we used the low-gain setup (up to 1.5 MeV) of the PIXIE ASIC.

6. Low-rate measurements

6.1. Room-temperature spectroscopic response

Fig. 5 shows an overview of the measured ^{241}Am spectra, at low rates (ICR < 600 cps), for array 3 (pixel pitch = 500 μm) and array 1 (pixel pitch = 250 μm). The spectra were measured at room temperature ($T = 25^\circ\text{C}$) and with a bias voltage of 1000 V (negative bias voltage at the cathode electrode), which is the optimum value at room temperature. This result highlights the good electrical characteristics of the detector (*i.e.* low leakage currents), which allow high bias voltage operation even at room temperature and with dc coupling to the electronics. In previous work (Allwork *et al.*, 2012; Veale *et al.*, 2011), commercial CZT pixel detectors with the same geometry, fabricated by Redlen Technologies, were investigated with this ASIC but working at lower bias voltages (less than 500 V) than our detector. Generally, the spectroscopic performance of the pixels of the large array (array 3) are better than the performance of the small array (array 1). The energy resolution (FWHM) values at 59.5 keV of the best pixels of the large and small arrays are 3.3% and 5%, respectively. This, despite the better unipolar behaviour of the weighting potential of the small array, is due to the strong effects of charge sharing in the small array, which is characterized by a higher G/A ratio. Charge-sharing effects are clearly visible in all spectra: (i) broadening of the energy peaks, (ii) tailing on the low-energy side of the main energy peaks, (iii) low energy background and (iv) fluorescent peaks (*e.g.* the Cd $K\alpha_1$ line at 23.2 keV).

6.2. Temperature effects

The performance of the detector arrays at different temperatures (down to $T = -5^\circ\text{C}$) was also investigated. Fig. 6 shows the measured ^{241}Am spectra for both arrays at different temperatures. Spectroscopic improvements were observed down to $T = 5^\circ\text{C}$, due to the reduction in the electronic noise (*i.e.* reduction in the leakage current of the detector). The slight resolution degradation at temperatures

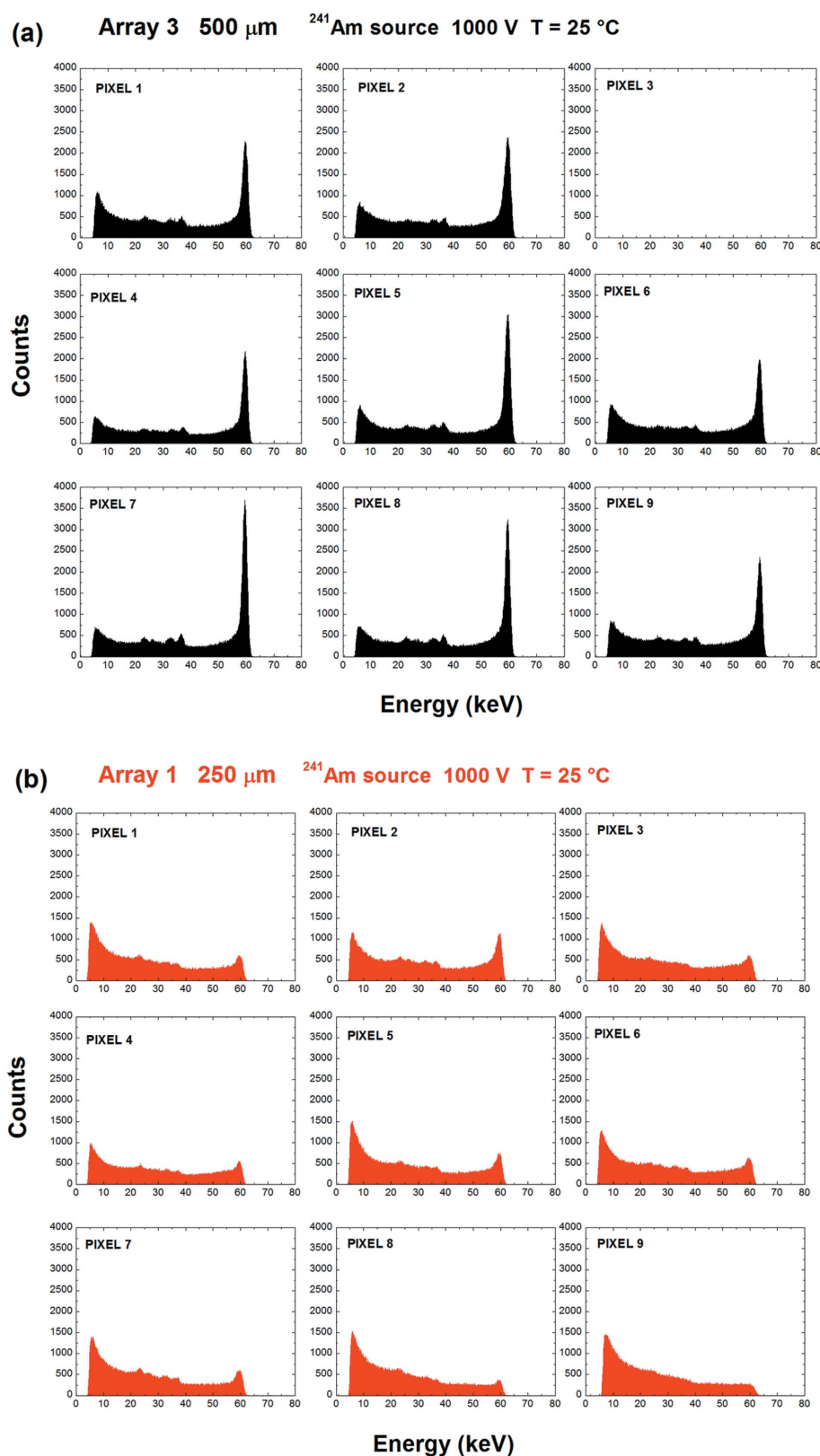


Figure 5

The measured ^{241}Am spectra of all pixels of (a) array 3 (ICR = 600 cps) and (b) array 1 (ICR = 200 cps) at room temperature. All spectra are characterized by the same total counts. (a) The energy resolution (FWHM) at 59.5 keV of the best pixel (pixel 7) and the sum of all spectra are 3.3 and 3.9%, respectively; the dead pixel (pixel 3) of array 3 is due to a failure in the flip-chip bonding. (b) The energy resolution (FWHM) at 59.5 keV of the best pixel (pixel 2) and the sum of all spectra are 5 and 7%, respectively.

below 5°C can be explained through a temperature perturbation of the electric field of the detector (mainly at the anode), typically observed in CZT detectors (Abbene *et al.*, 2016; Bale & Szeles, 2008; Sellin *et al.*, 2010). This is due to the formation of positive space charge in the bulk (accumulation of space charges at deep levels) that perturbs the electric field profile within the detector, producing poor charge drift. The low temperature delays the detrapping process and increases the charge buildup. We obtained the best performance at $T = 5^\circ\text{C}$ using a bias voltage of 1200 V, which is the maximum voltage fixed by the electronic components of the bias voltage filters. The ^{241}Am spectra for arrays 1 and 3, obtained by summing the individual spectra of all pixels (after energy calibration and equalization), are shown in Fig. 7. The energy resolution values at both 22.1 and 59.5 keV are reported in Table 3.

Table 3

Spectroscopic performance of the arrays at 1200 V and at $T = 5^\circ\text{C}$.

Array	Pixel	Energy resolution at 22.1 keV (%)	Energy resolution at 59.5 keV (%)
Array 3 (500 μm)	Best pixel (7)	7.7	3
Array 3 (500 μm)	Sum of all spectra	8.6	3.4
Array 1 (250 μm)	Best pixel (2)	10.1	3.7
Array 1 (250 μm)	Sum of all spectra	10.9	5

6.3. Time coincidence analysis (TCA) for charge-sharing detection

In this section, we investigate the detection of charge-sharing events through TCA, *i.e.* by detecting the events of the central pixel (pixel 5) that are in temporal coincidence with adjacent pixels, within selected CTWs. The digital system allows fine TCA with CTWs up to 10 ns. Preliminary measurements concerned investigations of the temperature dependence of the number of shared events with the ^{241}Am source. Using a bias voltage of 1000 V and an energy threshold of 4 keV, we measured, for each array, the events of the central pixel (pixel 5) which are in temporal coincidence (CTW = 450 ns) with adjacent pixels. The 4 keV energy threshold represents the optimum value for no noise detection within the investigated temperature range of 25 to -5°C . Generally, we did not observe significant changes in the number of shared events down to $T = -5^\circ\text{C}$. In particular, we measured a slight increase in shared events on lowering the temperature. For example concerning the large array (array 3), the percentages of shared events are 55% and 59% at $T = 25^\circ\text{C}$ and $T = -5^\circ\text{C}$, respectively. This increase is probably due to the perturbation of the electric field profile created by lowering the temperature, as discussed before. Moreover, concerning the broadening of the electron cloud due to diffusion, very small changes are expected at 59.5 keV from equation (1): $s = 31 \mu\text{m}$ and $s = 30 \mu\text{m}$ at $T = 25^\circ\text{C}$ and $T = -5^\circ\text{C}$, respectively.

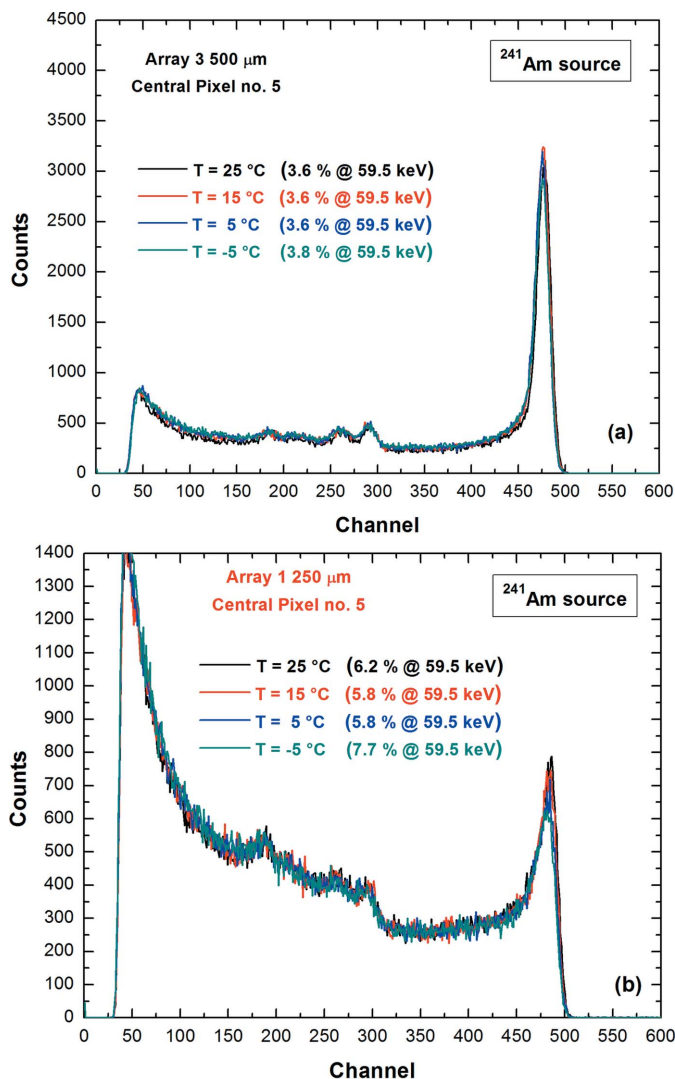


Figure 6 The measured ^{241}Am spectra of the central pixel (pixel 5) at different temperatures for (a) the large array and (b) the small array. A bias voltage of 1000 V was used.

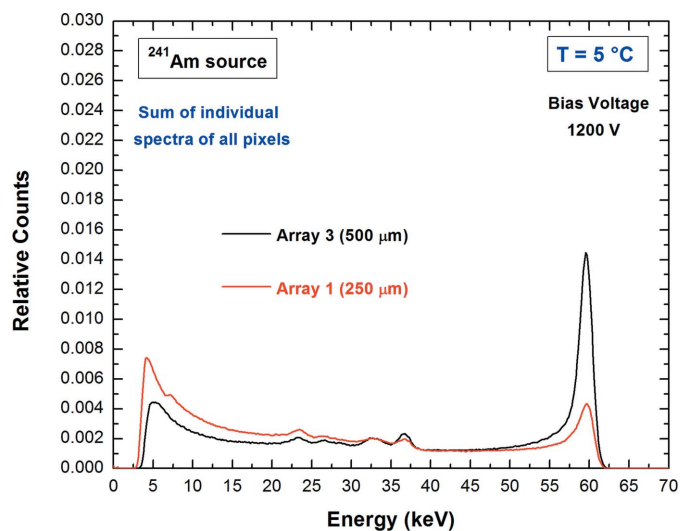


Figure 7 The sum of the individual ^{241}Am spectra of all pixels, after energy calibration and equalization, of the two arrays at 1200 V ($T = 5^\circ\text{C}$). The spectra are normalized to the total counts.

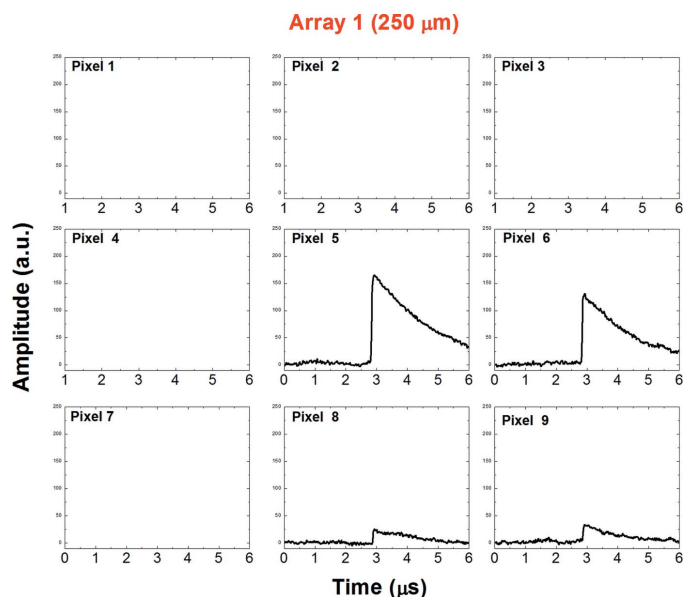


Figure 8
Typical charge-sharing event (^{241}Am source) involving four pixels of array 1. The pulses are in temporal coincidence within a CTW of 10 ns.

In the following, all charge-sharing measurements were performed at $T = 5^\circ\text{C}$ with a bias voltage of 1200 V and an energy threshold of 3 keV. Fig. 8 shows the CSP output pulses related to a typical charge-sharing event (^{241}Am source) involving four pixels (event multiplicity $m = 4$) of array 1 ($250\ \mu\text{m}$), within a CTW of 10 ns. The shape of the CSP output pulses is typical of collected-charge pulses and no pure transient pulses were observed. Probably, the non-zero energy threshold (3 keV) and the relatively low energy range (up to 60 keV) do not allow the detection of transient pulses, which are typically characterized by small amplitudes. In the literature (Brambilla *et al.*, 2012; Bolotnikov *et al.*, 2016; Kim *et al.*, 2011), the detection of these events has been presented at

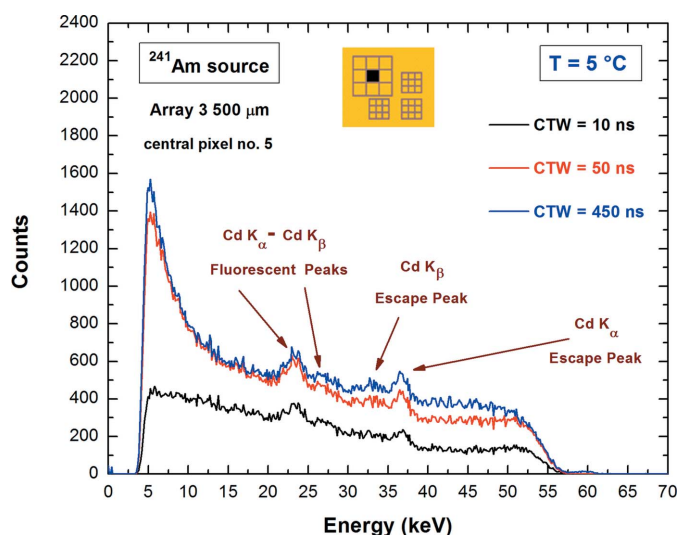


Figure 9
The energy spectra of the events of central pixel 5 (large array 3) that are in coincidence with the other adjacent pixels at three different CTWs. Examples of fluorescent and escape peaks are clearly visible.

higher energies (e.g. 122 and 662 keV). Fig. 9 shows the energy distributions (i.e. the energy spectra) of the events of the central pixel of array 3 in temporal coincidence with other adjacent pixels, at three different CTWs. Examples of fluorescent and escape peaks are clearly visible. Fig. 10(a) shows the number of shared events of central pixel 5 at different CTWs, ranging from 10 to 600 ns, and at different energies (^{109}Cd and ^{241}Am). The saturation of the curves in Fig. 10(a) clearly shows full detection of the shared events within the investigated CTW range. The event multiplicity m , referred to the number of pixels involved in a charge-sharing detection, is reported in Fig. 10(b). Firstly, these measurements clearly show the difference in charge sharing between the two arrays. Due to the higher G/A ratio (Table 1), the small array (array 1) is characterized by more charge sharing; moreover, the differences in charge sharing between the energies below

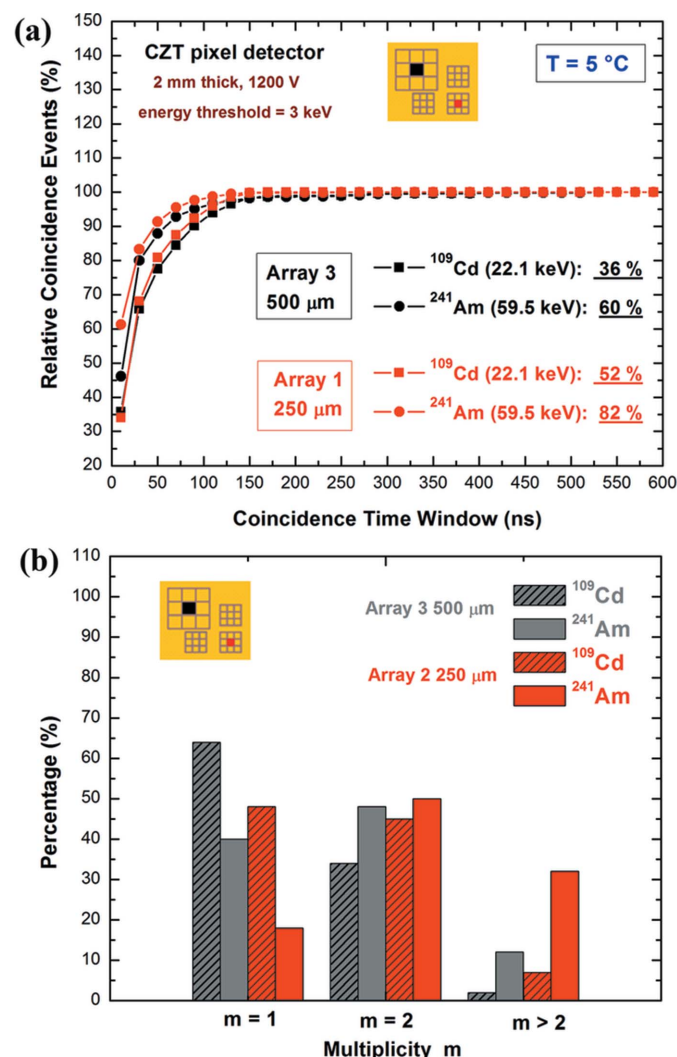


Figure 10
(a) Relative coincidence events (percentage) of central pixel 5 for arrays 3 and 1 with adjacent pixels at different CTWs and energies (^{109}Cd and ^{241}Am). An energy threshold of 3 keV for all pixels was used. The percentage values of the coincidence events of pixel 5 with all pixels, for both energies and arrays, are also shown (CTW of 450 ns). (b) The event multiplicity m relative to the number of pixels involved in a charge-sharing detection.

Table 4

Measured and calculated percentages of the number of charge-shared events between two adjacent pixels (5 and 8) of arrays 1 and 3.

A bias voltage of 1200 V at $T = 5^\circ\text{C}$ and energy threshold of 3 keV were used.

Array	Radioactive source	Shared events between two adjacent pixels (%) (measured)	Shared events between two adjacent pixels (%) [calculated from equation (2)]
Array 3 (500 μm)	^{109}Cd	9	11
Array 3 (500 μm)	^{241}Am	16	11
Array 1 (250 μm)	^{109}Cd	19	22
Array 1 (250 μm)	^{241}Am	28	22

(^{109}Cd) and above (^{241}Am) the K -shell absorption energy of the CZT material, highlight the critical role of X-ray fluorescence.

In order to give a validation for the number of detected shared events, we also measured the shared events between two adjacent pixels and we compared the results with the percentages expected from equation (2). The results are

shown in Table 4. Generally, good agreement is obtained between the measured and calculated percentages with the ^{109}Cd source, *i.e.* with energies below the K -shell absorption energy of the CZT material that do not create fluorescent X-rays. The measured percentages with the ^{109}Cd source are always less than the calculated ones, due to the non-zero energy threshold of the processing analysis (3 keV). On the contrary, the results with the ^{241}Am source highlight a greater discrepancy between the measured and calculated values and the measured percentages are greater than the calculated ones. This disagreement is due to the presence of X-ray fluorescence with the ^{241}Am source, which is not taken into account in equation (2).

The improvements in the energy spectra after CSD are shown in Fig. 11. In particular, we present three different spectra of the central pixel for each array and energy: (i) the raw spectra of the central pixel after energy calibration (black line); (ii) the spectra of the coincidence events with all adjacent pixels with a CTW of 450 ns (red line); and (iii) the spectra after CSD. It can clearly be seen that there is a strong reduction in the shared events in the spectra after CSD. The

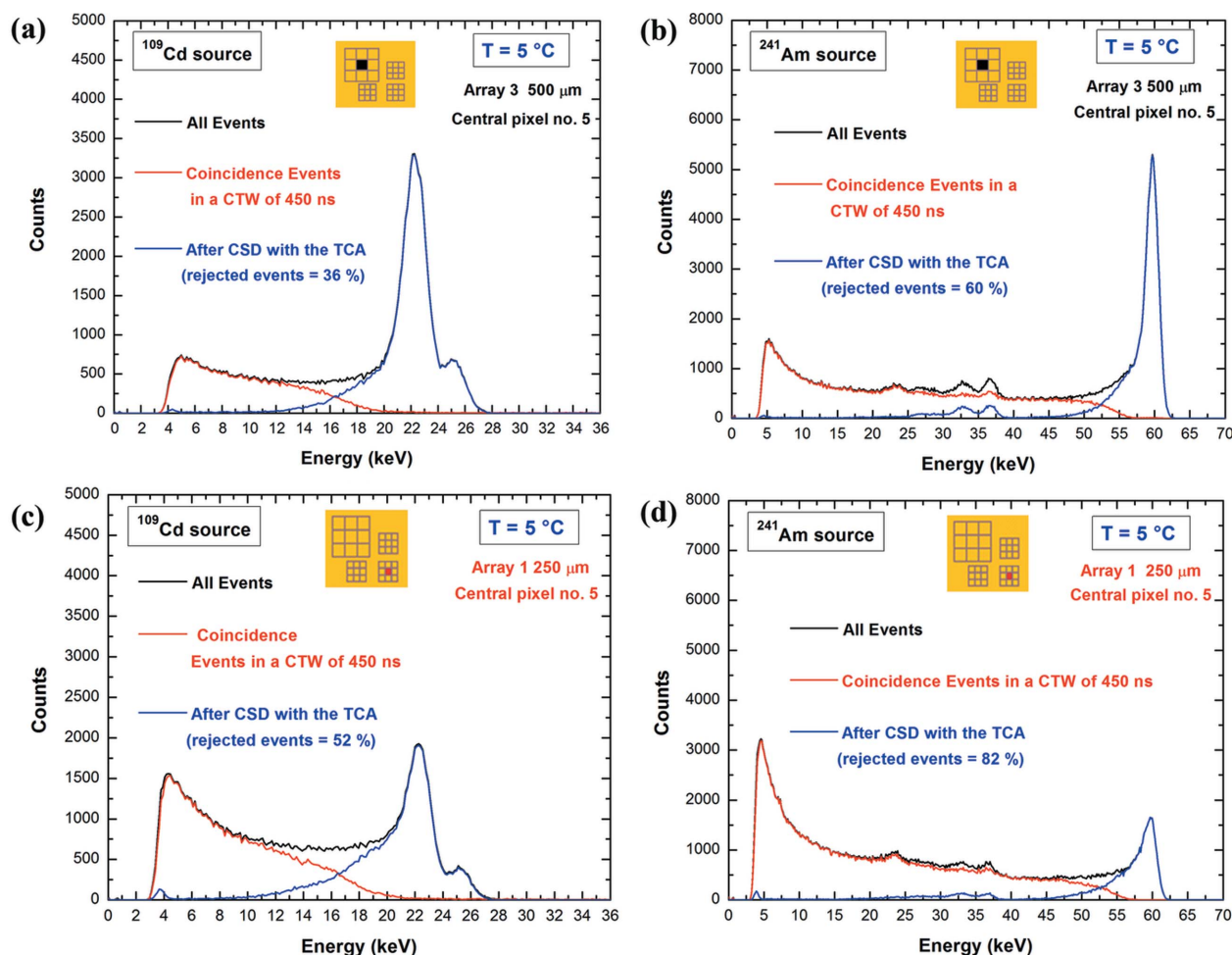


Figure 11

The raw spectra of central pixel 5 (black line), and the spectra of the coincidence events with all adjacent pixels (red line) and after CSD (blue line). The spectra were measured for the central pixel of both arrays: (a) and (b) array 3, and (c) and (d) array 1. The strong reduction of the shared events after CSD is clearly visible. Concerning the energy resolution, no improvements were obtained after CSD. The energy resolution values of central pixel 5 are: (i) for array 3, 9.5 and 3.6% at 22.1 and 59.5 keV, respectively; (ii) for array 1, 11.3 and 5.2% at 22.1 and 59.5 keV, respectively.

low-energy side of the raw spectra perfectly coincides with the coincidence spectra (*i.e.* the spectra of the shared events) and the fluorescence X-rays are deleted after CSD. Some escape peaks are present in the ^{241}Am spectra even after CSD, due to back escape events (*e.g.* from the cathode side) and fluorescence events absorbed beyond the adjacent pixels (*i.e.* absorbed below the guard-ring electrode). With the energy threshold used in the sharing detection (3 keV), no improvements in the energy resolution of the main peaks were obtained after CSD.

6.4. Charge losses after charge-sharing addition (CSA)

To recover the shared events rejected by the CSD, the CSA technique is typically applied (Allwork *et al.*, 2012; Kuvvetli *et al.*, 2007; Meuris *et al.*, 2009; Veale *et al.*, 2014b). The spectra of the coincidence events, between pixel 5 and the adjacent pixels, after CSA are shown in Fig. 12. The spectra are obtained by summing the energies of the events of the central pixel 5 with the energies of the other pixels that are in temporal coincidence (CTW = 450 ns). Besides the worsening

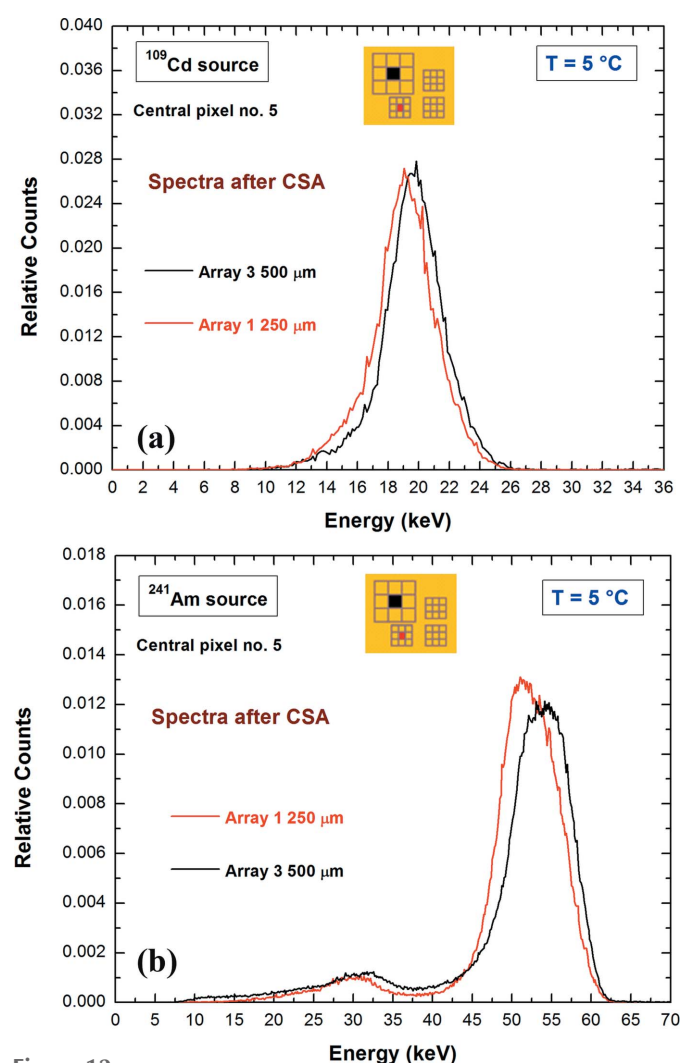


Figure 12 The spectra of the coincidence events between pixel 5 and the adjacent pixels of arrays 1 and 3, after CSA. (a) ^{109}Cd and (b) ^{241}Am sources.

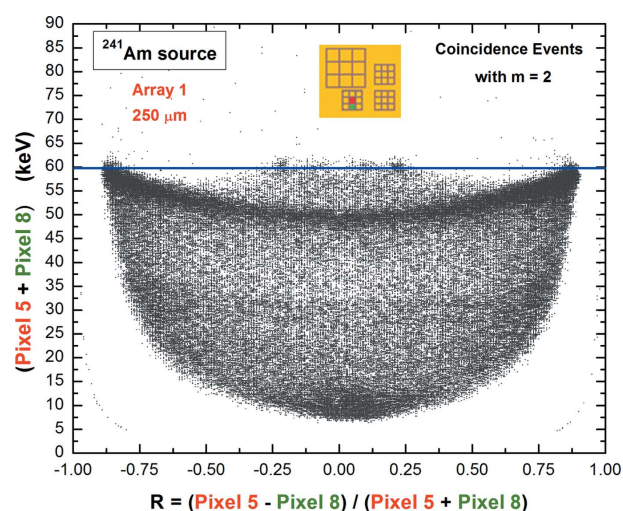


Figure 13 Two-dimensional scatter plot of the summed coincidence events ($m = 2$) between pixels 5 and 8 *versus* the ratio R , which gives information on the interaction position of the events. The shift of the track to lower energies than 59.5 keV (blue line) clearly highlights the presence of charge losses near the inter-pixel region. The two kinks at $R = \pm 0.22$ are due to the escape of fluorescent X-rays from the CZT material (*e.g.* the Cd $K\alpha_1$ fluorescent line is characterized by an energy of 23.2 keV).

of the energy resolution, the spectra are also characterized by a reduction of the centroid of the main peaks, *i.e.* by charge losses. This effect is more severe for the 250 μm array (array 1), with a maximum charge loss of about 13% (8 keV) for array 1 at the 59.5 keV line (^{241}Am source). As discussed before, charge losses after CSA have been already observed in pixellated CZT detectors (Allwork *et al.*, 2012; Bolotnikov *et al.*, 1999, 2002; Gaskin *et al.*, 2003; Kalemci & Matteson, 2002; Kuvvetli *et al.*, 2007). Unfortunately, under our experimental conditions (uncollimated irradiation), we cannot give a precise interpretation of these losses, which can be related to the non-zero energy threshold of the electronics, the electric field distortions and/or weighting cross-talk effects near the inter-pixel gap.

Fig. 13 shows charge-loss effects *versus* the interaction positions of shared events, between two adjacent pixels (pixels 5 and 8) of the 250 μm array (array 1). Information about the interaction position of the shared events is obtained from the ratio R between the energy of the pixel events: (pixel 5 – pixel 8)/(pixel 5 + pixel 8). The curvature shows that the shared events do not have 100% efficient charge collection and that charge losses are more severe for those events which are stopped in the middle of the inter-pixel gap. The two kinks at $R = \pm 0.22$ are due to the escape of fluorescent X-rays from the CZT material (Table 2). No kinks with energies greater than 60 keV, due to the addition of a collected-charge pulse with a false induced charge in a neighbouring pixel, are observed in Fig. 13. This confirms the detection of no pure transient events.

6.5. Pulse shape analysis (PSA) for charge-sharing detection

We also investigated a possible relation between the shapes of the pulses and the charge-sharing events. As discussed

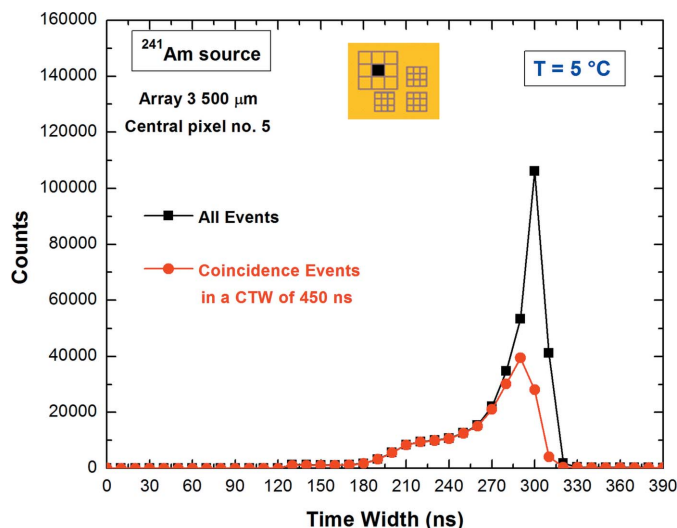


Figure 14
The TW distribution (with time bin widths of 10 ns) of the coincidence pulses (^{241}Am) of central pixel 5 with all adjacent pixels (red line). The black line represents the TW distribution of all events of pixel 5. At TWs < 290 ns, the percentage of charge-sharing events is >90%. This result opens up the use of the PSD technique to reject charge-sharing events.

before, the digital system is also able to estimate the pulse shape of fast SDL pulses, represented by the time width (TW) of each pulse. Due to the characteristics of the SDL shaping, the time width of the SDL pulses is generally related to the time delay of the SDL shaping and to the peaking time of the CSP output pulses. Fig. 14 shows the TW distribution (red line), with a time bin of 10 ns, of the coincidence pulses (^{241}Am) of central pixel 5 with all adjacent pixels of the 500 μm pitch array (array 3). The distribution clearly highlights the strong relation between the TWs of the pulses (*i.e.* the pulse shape) and the shared events. In particular, at TWs < 290 ns, the percentage of charge-sharing events is >90%. This

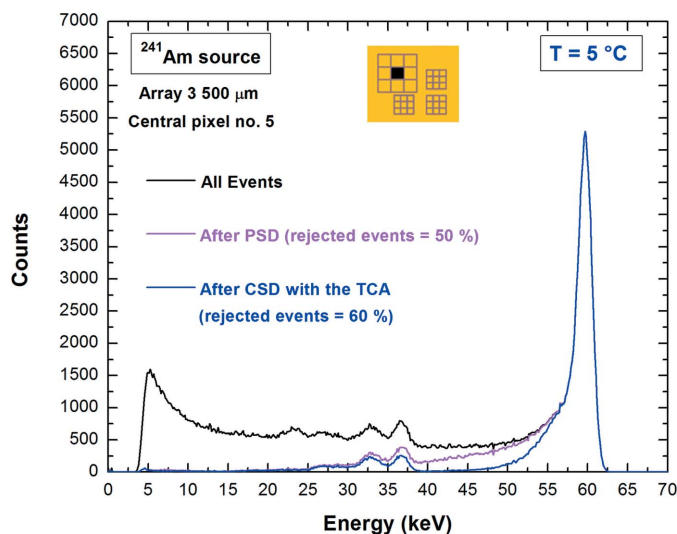


Figure 15
The ^{241}Am spectrum (magenta line) of central pixel 5 after PSD, the spectrum after CSD with the TCA (blue line) and the raw spectrum with all events (black line). The PSD does not recognize shared events (about 10% of all events) between the 59.5 keV peak and the 36.3 keV escape peak.

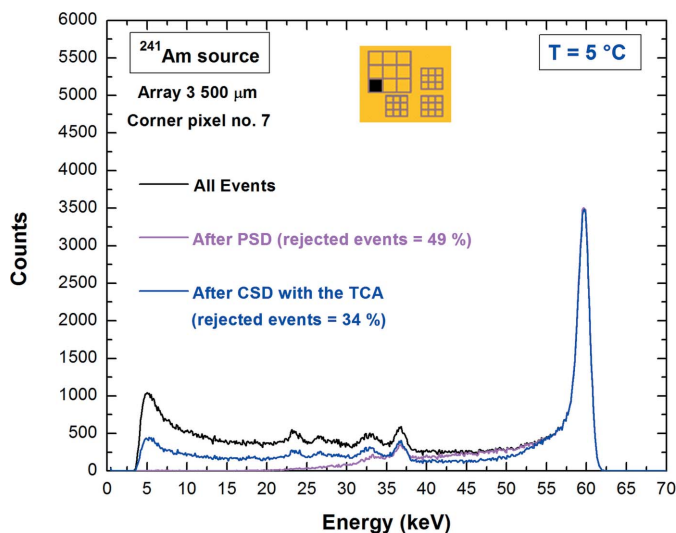


Figure 16
The ^{241}Am spectrum (magenta line) of a corner pixel (pixel 7) after PSD, the spectrum after CSD with the TCA (blue line) and the raw spectrum with all events (black line).

result opens up the use of the pulse shape discrimination (PSD) technique for the rejection of charge-sharing events. Indeed, Fig. 15 highlights the results of the PSD for the rejection of charge-sharing events (magenta line). The raw spectrum (black line) and the spectrum after CSD (blue line) are also shown. We selected a time width region (TWR) able to produce no reduction in counts in the main photopeak centroid (59.5 keV) of the spectrum (290 < TW < 320 ns). Only a fraction of about 10% of all events, located between the 59.5 keV peak and the 36.3 keV escape peak, are not detected by the PSA, because these events are characterized by similar peaking times to the correct pulses. The PSA can be also helpful for detecting shared events in pixels that are not completely surrounded by other pixels, such as border and corner pixels. The results of the detection of charge sharing in a corner pixel of array 3, using both PSD and CSD, are reported in Fig. 16. In this case, PSD performs a better recognition of the shared events than that obtained using CSD with TCA.

7. High-rate measurements

The spectroscopic response of the detector to the ^{241}Am source at high rates (ICR of 250 kcps per pixel) was also investigated. This counting rate is not the limiting value for the system but represents the maximum value obtained with the ^{241}Am source (*i.e.* the counting rate was limited by the source activity). However, this rate condition allowed us to show the typical critical issues at high rates and our solutions to them.

The digital system is characterized by a dead-time of 300 ns and an output counting rate (OCR) of 232 kcps (throughput of 93%). The measured spectra of the central pixel at both low and high ICRs are shown in Fig. 17(a). Low shifts of the peaks (<0.5%) and low degradation of the energy resolution were observed. This is due to the short TWs of the fast shaped pulses and to the effect of baseline restoration. Concerning the

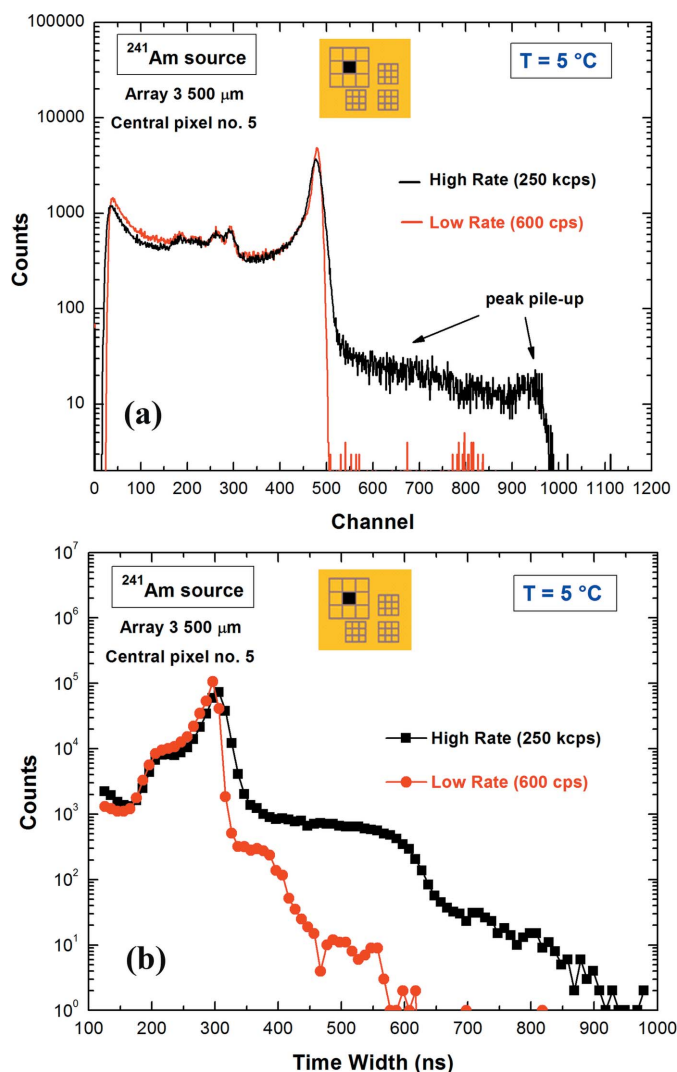


Figure 17
 (a) The ^{241}Am spectra measured at both low and high ICRs. The energy resolutions at 59.5 keV (FWHM) are 3.6 and 5% at low and high ICRs, respectively. (b) The TW distribution at low and high ICRs.

TW distributions of Fig. 17(b), the curve at high ICR is characterized by a tail on the high TW side, due to the peak pile-up events. Therefore, proper choice of the TW region allows the rejection of both charge-sharing and pile-up events. Concerning the detection of charge sharing at high rates, Fig. 18(a) clearly shows that, as the TCA fails at high rates, the number of coincidence events does not saturate at $\text{CTW} > 450\ \text{ns}$ (blue curve), contrary to what happens at low rates (red curve). At high rates, false shared events are present, *i.e.* coincidence events due to photons interacting simultaneously on neighbouring pixels. The energy distribution of the coincidence pulses (Fig. 18b) highlights the presence of false-shared events even at a coincidence time window of 10 ns. The results of the PSD technique are shown in Fig. 19: by selecting a proper TWR, PSD allows a better discrimination of shared events at high ICRs. The PSD technique is able to detect 83% of the shared events, while the CSD, used with a short CTW of 10 ns in order to minimize the detection of false shared events

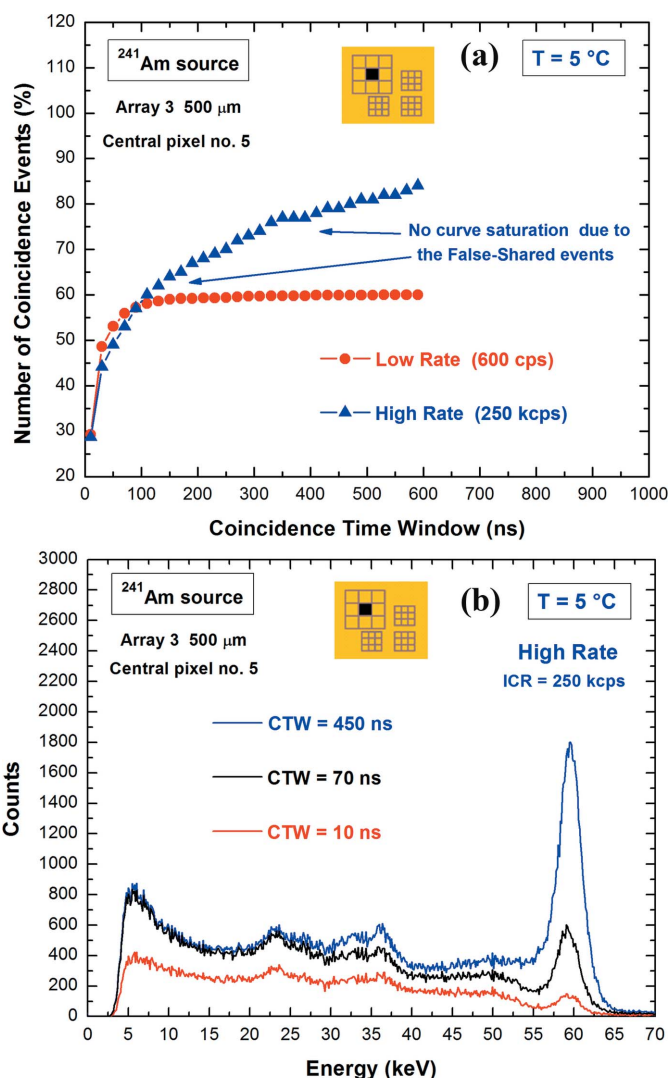


Figure 18
 (a) Coincidence events (percentage) for central pixel 5 with other adjacent pixels at different CTWs and at both low (circles) and high (triangles) rate conditions. Due to the high rate condition, the blue curve does not saturate. (b) High rate coincidence spectra at different CTWs. This result clearly shows that the coincidence technique fails at high ICRs, due to the presence of false-shared events, *i.e.* coincidence events due to photons interacting simultaneously on neighbouring pixels. The energy distribution of the coincidence events highlights the presence of false shared events, even at a CTW of 10 ns.

at 59.5 keV, allows the detection of only 48% of the shared events.

8. Conclusions

The performance of a digital CZT detector prototype for high-flux X-ray spectroscopic imaging has been presented in this work. The CZT pixel detector (2 mm thick) is characterized by arrays with pixel pitches of 500 and 250 μm and dc coupled to a low-noise ASIC, allowing good spectroscopic performance and high bias voltage operation (5000 V cm^{-1}), even at room temperature. The detector signals are processed by custom digital real-time electronics able to perform low dead-time

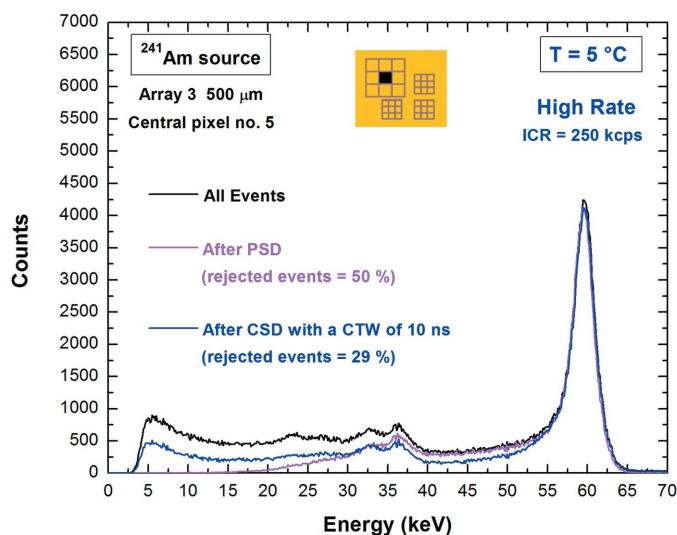


Figure 19
The ^{241}Am spectrum at 250 kcps (magenta line) of central pixel 5 after PSD. The spectra after CSD with a CTW of 10 ns (blue line) and with all events (black line) are also shown. The PSD allows a better discrimination of the shared events at high rates.

energy measurements with reasonable resolution using fine TCA and PSA at both low and high rates. Using digital fast shaping analysis (with a dead-time of 300 ns), the energy resolutions, at moderate cooling ($T = 5^\circ\text{C}$), are roughly 3.5% and 5% at 59.5 keV for the large (500 μm) and small arrays (250 μm), respectively, with slight degradations at high rates (up to 250 kcps per pixel).

Charge-sharing investigations were performed using both the TCA, with coincidence time windows (CTWs) up to 10 ns, and the PSA. Measurements with photon energies below (^{109}Cd source) and above (^{241}Am source) the K -shell absorption energy of the CZT material highlight the strong influence of X-ray fluorescence on the number of shared events. At the optimum experimental conditions ($T = 5^\circ\text{C}$, 1200 V and an energy threshold of 3 keV), the central pixel of the 500 μm array (250 μm array) is in temporal coincidence with adjacent pixels with percentages of 36% (52%) and 60% (82%) at 22.1 and 59.5 keV, respectively.

The CSD with TCA and the PSD techniques were compared in charge-sharing detection. Despite the fact that the PSD did not recognize about 17% of shared events, better results were obtained with the PSD for corner/border pixels and at high rates, where the CSD with the TCA fails. CSA was also applied, showing critical issues in the recovery of shared events, due to charge losses in the inter-pixel gap.

Further investigations with collimated synchrotron X-ray beams are foreseen, with the goal of better understanding the effects of beam position on the pulse height, the pulse shape and the multiplicity of events.

Acknowledgements

The authors would like to acknowledge the technical staff of the laboratory at DiFC of Palermo, Mr Marcello Mirabello, for his technical assistance. The authors would also like to

acknowledge the technical staff of the Interconnect team who performed the bonding of the detectors at the Rutherford Appleton Laboratory, Dr Andreas Schneider and Mr Paul Booker.

Funding information

Funding for this research was provided by: Ministero dell'Istruzione, dell'Università e della Ricerca (PRIN Project No. 2012WM9MEP); Science and Technology Facilities Council (UK) under the Centre for Instrumentation Sensors Managed Programme 2016–2017.

References

Abbene, L., Del Sordo, S., Fauci, F., Gerardi, G., La Manna, A., Raso, G., Cola, A., Perillo, E., Raulo, A., Gostilo, V. & Stumbo, S. (2007). *Nucl. Instrum. Methods Phys. Res. A*, **583**, 324–331.

Abbene, L. & Gerardi, G. (2015). *J. Synchrotron Rad.* **22**, 1190–1201.

Abbene, L., Gerardi, G. & Principato, F. (2013). *Nucl. Instrum. Methods Phys. Res. A*, **730**, 124–128.

Abbene, L., Gerardi, G. & Principato, F. (2015). *Nucl. Instrum. Methods Phys. Res. A*, **777**, 54–62.

Abbene, L., Gerardi, G., Raso, G., Principato, F., Zambelli, N., Benassi, G., Bettelli, M. & Zappettini, A. (2017). *J. Synchrotron Rad.* **24**, 429–438.

Abbene, L., Gerardi, G., Turturici, A. A., Raso, G., Benassi, G., Bettelli, M., Zambelli, N., Zappettini, A. & Principato, F. (2016). *Nucl. Instrum. Methods Phys. Res. A*, **835**, 1–12.

Allwork, C., Kitou, D., Chaudhuri, S., Sellin, P. J., Seller, P., Veale, M. C., Tartoni, N. & Veeramani, P. (2012). *IEEE Trans. Nucl. Sci.* **59**, 1563–1568.

Awadalla, S. A., Al-Grafi, M. & Iniewski, K. (2014). *Nucl. Instrum. Methods Phys. Res. A*, **764**, 193–197.

Bale, D. S. & Szeles, C. (2008). *Phys. Rev. B*, **77**, 035205.

Barber, W. C., Wessel, J. C., Nygard, E. & Iwanczyk, J. S. (2015). *Nucl. Instrum. Methods Phys. Res. A*, **784**, 531–537.

Barret, H. H., Eskin, J. D. & Barber, H. B. (1995). *Phys. Rev. Lett.* **75**, 156–159.

Baumer, C., Martens, G., Menser, B., Roessl, E., Schломka, J., Steadman, R. & Zeitler, G. (2008). *IEEE Trans. Nucl. Sci.* **55**, 1785–1790.

Benassi, G., Nasi, L., Bettelli, M., Zambelli, N., Calestani, D. & Zappettini, A. (2017). *J. Instrum.* **12**, P02018.

Berger, M. J., Hubbell, J. H., Seltzer, S. M., Chang, J., Coursey, J. S., Sukumar, R., Zucker, D. S. & Olsen K. (1998). *Xcom: Photon Cross Section Database*, <https://www.nist.gov/pml/xcom-photon-cross-sections-database>.

Bertuccio, G., Ahangarianabbaria, M., Graziani, C., Macera, D., Shi, Y., Rachevski, A., Rashevskaya, I., Vacchi, A., Zampa, G., Zampa, N., Bellutti, P., Giacomini, G., Picciotto, A. & Piemonte, C. (2015). *J. Instrum.* **10**, P01002.

Bolotnikov, A. E., Bale, D., Butcher, J., Camarda, G. S., Cui, Y., De Geronimo, G., Fried, J., Hossain, A., Kim, K. H., Marshall, M., Soldner, S., Petryk, M., Prokesch, M., Vernon, E., Yang, G. & James, R. B. (2014). *IEEE Trans. Nucl. Sci.* **61**, 787–792.

Bolotnikov, A. E., Boggs, S. E., Hubert Chen, C. M., Cook, W. R., Harrison, F. A. & Schindler, S. M. (2002). *Nucl. Instrum. Methods Phys. Res. A*, **482**, 395–407.

Bolotnikov, A. E., Camarda, G. S., Carini, G. A., Cui, Y., Li, L. & James, R. B. (2007). *Nucl. Instrum. Methods Phys. Res. A*, **571**, 687–698.

Bolotnikov, A. E., Camarda, G. S., Cui, Y., De Geronimo, G., Eger, J., Emerick, A., Fried, J., Hossain, A., Roy, U., Salwen, C., Soldner, S., Vernon, E., Yang, G. & James, R. B. (2016). *Nucl. Instrum. Methods Phys. Res. A*, **805**, 41–54.

- Bolotnikov, A. E., Cook, W. R., Harrison, F. A., Wong, A.-S., Schindler, S. M. & Eichelberger, A. C. (1999). *Nucl. Instrum. Methods Phys. Res. A*, **432**, 326–331.
- Brambilla, A. *et al.* (2009). *IEEE Nucl. Sci. Symp. Conf. Rec.* **5402215**, 1753–1757.
- Brambilla, A., Ouvrier-Buffet, P., Gonon, G., Rinkel, J., Moulin, V., Boudou, C. & Verger, L. (2013). *IEEE Trans. Nucl. Sci.* **60**, 408–415.
- Brambilla, A., Ouvrier-Buffet, P., Rinkel, J., Gonon, G., Boudou, C. & Verger, L. (2012). *IEEE Trans. Nucl. Sci.* **59**, 1552–1558.
- Campbell, D. L. *et al.* (2013). *IEEE Nucl. Sci. Symp. Conf. Rec.* **6829172**, 1–6.
- Chen, C. M. H., Boggs, S. E., Bolotnikov, A. E., Cook, W. R., Harrison, F. A. & Schindler, S. M. (2002). *IEEE Trans. Nucl. Sci.* **49**, 270–276.
- Chen, H. *et al.* (2008). *J. Appl. Phys.* **103**, 014903.
- Chen, H., Awadalla, S. A., Mackenzie, J., Redden, R., Bindley, G., Bolotnikov, A. E., Camarda, G. S., Carini, G. & James, R. B. (2007). *IEEE Trans. Nucl. Sci.* **54**, 811–816.
- Del Sordo, S., Abbene, L., Caroli, E., Mancini, A. M., Zappettini, A. & Ubertini, P. (2009). *Sensors*, **9**, 3491–3526.
- Gaskin, J. A., Sharma, D. P. & Ramsey, B. D. (2003). *Nucl. Instrum. Methods Phys. Res. A*, **505**, 122–125.
- Gatti, E. & Rehak, P. (1984). *Nucl. Instrum. Methods Phys. Res.* **225**, 608–614.
- Gatti, E., Rehak, P. & Walton, J. T. (1984). *Nucl. Instrum. Methods Phys. Res. A*, **226**, 129–141.
- Gerardi, G. & Abbene, L. (2014). *Nucl. Instrum. Methods Phys. Res. A*, **768**, 46–54.
- Greenberg, J. A., Hassan, M., Brady, D. J. & Iniewski, K. (2016). *Proc. SPIE*, **9847**, 98470E.
- Guerra, P., Santos, A. & Darambara, D. G. (2008). *Phys. Med. Biol.* **53**, 1099–1113.
- He, Z. (2001). *Nucl. Instrum. Methods Phys. Res. A*, **463**, 250–267.
- Iniewski, K. *et al.* (2007). *IEEE Nucl. Sci. Symp. Conf. Rec.* **4437135**, 4608–4611.
- Iwaczyk, J., Nygård, E., Meirav, O., Arenson, J., Barber, W. C., Hartsough, N. E., Malakhov, N. & Wessel, J. C. (2009). *IEEE Trans. Nucl. Sci.* **56**, 535–542.
- Johnson, L. C., Ovchinnikov, O., Shokouhi, S. & Peterson, T. E. (2015). *IEEE Trans. Nucl. Sci.* **62**, 2036–2042.
- Kalemci, E. & Matteson, J. L. (2002). *Nucl. Instrum. Methods Phys. Res. A*, **478**, 527–537.
- Kim, J. C., Anderson, S. E., Kaye, W., Zhang, F., Zhu, Y., Kaye, S. J. & He, Z. (2011). *Nucl. Instrum. Methods Phys. Res. A*, **654**, 233–243.
- Kim, J. C., Kaye, W. R. & He, Z. (2014). *J. Korean Phys. Soc.* **64**, 1336–1345.
- Knoll, G. F. (2000). *Radiation Detection and Measurement*, ch. 4. New York: John Wiley and Sons.
- Krings, T., Spillmann, U., Protić, D., Roß, C., Stöhlker, Th., Weber, G., Bombelli, L., Alberti, R. & Frizzi, T. (2015). *J. Instrum.* **10**, C02043.
- Kuvvetli, I. *et al.* (2007). *IEEE Nucl. Sci. Symp. Conf. Rec.* pp. 2252–2257.
- Mardor, I., Shor, A. & Eisen, Y. (2001). *IEEE Trans. Nucl. Sci.* **48**, 1033–1040.
- Meuris, A., Limousin, O. & Blondel, C. (2009). *Nucl. Instrum. Methods Phys. Res. A*, **610**, 294–297.
- Norlin, B., Frojdh, C., Thungstrom, G. & Greiffenberg, D. (2008). *IEEE Nucl. Sci. Symp. Conf. Rec.* **4775083**, 3464–3469.
- Ogawa, K., Kobayashi, T., Kaibuki, F., Yamakawa, T., Nagano, T., Hashimoto, D. & Nagaoka, H. (2012). *Nucl. Instrum. Methods Phys. Res. A*, **664**, 29–37.
- Owens, A. & Peacock, A. (2004). *Nucl. Instrum. Methods Phys. Res. A*, **531**, 18–37.
- Ramo, S. (1939). *Proc. IRE*, **27**, 584.
- Schneider, A., Veale, M. C., Duarte, D. D., Bell, S. J., Wilson, M. D., Lippa, J. D. & Seller, P. (2015). *J. Instrum.* **10**, C02010.
- Sellin, P. J., Prekas, G., Franc, J. & Grill, R. (2010). *Appl. Phys. Lett.* **96**, 133509.
- Shikhaliyev, P. M., Fritz, S. G. & Chapman, J. W. (2009). *Med. Phys.* **36**, 5107–5119.
- Shockley, W. (1938). *J. Appl. Phys.* **9**, 635–636.
- Strassburg, M., Schroeter, C. & Hackenschmied, P. (2011). *J. Instrum.* **6**, C01055.
- Streicher, M., Zhu, Y. & He, Z. (2015). *IEEE Nucl. Sci. Symp. Conf. Rec.* **7582262**, 1–4.
- Szeles, C., Soldner, S. A., Vydrin, S., Graves, J. & Bale, D. S. (2008). *IEEE Trans. Nucl. Sci.* **55**, 572–582.
- Taguchi, K., Frey, E. C., Wang, X., Iwaczyk, J. S. & Barber, W. C. (2010). *Med. Phys.* **37**, 3957–3969.
- Taguchi, K. & Iwaczyk, J. S. (2013). *Med. Phys.* **40**, 100901.
- Takahashi, T. & Watanabe, S. (2001). *IEEE Trans. Nucl. Sci.* **48**, 950–959.
- Tomita, Y. *et al.* (2004). *IEEE Nucl. Sci. Symp. Conf. Rec.* **6**, 3733–3737.
- Veale, M. C. *et al.* (2014a). *J. Instrum.* **9**, C12047.
- Veale, M. C., Bell, S. J., Duarte, D. D., Schneider, A., Seller, P., Wilson, M. D. & Iniewski, K. (2014b). *Nucl. Instrum. Methods Phys. Res. A*, **767**, 218–226.
- Veale, M. C., Bell, S. J., Jones, L. L., Seller, P., Wilson, M. D., Allwork, C., Kitou, D., Sellin, P. J., Veeramani, P. & Cernik, R. C. (2011). *IEEE Trans. Nucl. Sci.* **58**, 2357–2362.
- Xu, C. *et al.* (2011). *IEEE Trans. Nucl. Sci.* **58**, 614–625.